

REPORT DOCUMENTATION PAGE				Form Approved OMB NO. 0704-0188	
<p>The public reporting burden for this collection of information is estimated to average 1 hour per response, including the time for reviewing instructions, searching existing data sources, gathering and maintaining the data needed, and completing and reviewing the collection of information. Send comments regarding this burden estimate or any other aspect of this collection of information, including suggestions for reducing this burden, to Washington Headquarters Services, Directorate for Information Operations and Reports, 1215 Jefferson Davis Highway, Suite 1204, Arlington VA, 22202-4302. Respondents should be aware that notwithstanding any other provision of law, no person shall be subject to any penalty for failing to comply with a collection of information if it does not display a currently valid OMB control number.</p> <p>PLEASE DO NOT RETURN YOUR FORM TO THE ABOVE ADDRESS.</p>					
1. REPORT DATE (DD-MM-YYYY) 19-08-2010		2. REPORT TYPE Final Report		3. DATES COVERED (From - To) 1-May-2007 - 30-Apr-2010	
4. TITLE AND SUBTITLE Enhanced nonlinear optical devices using artificial slow-light structures				5a. CONTRACT NUMBER W911NF-07-1-0245	
				5b. GRANT NUMBER	
				5c. PROGRAM ELEMENT NUMBER 611102	
6. AUTHORS Steve Blair				5d. PROJECT NUMBER	
				5e. TASK NUMBER	
				5f. WORK UNIT NUMBER	
7. PERFORMING ORGANIZATION NAMES AND ADDRESSES University of Utah Office of Sponsored Programs University of Utah Salt Lake City, UT 84102 -				8. PERFORMING ORGANIZATION REPORT NUMBER	
9. SPONSORING/MONITORING AGENCY NAME(S) AND ADDRESS(ES) U.S. Army Research Office P.O. Box 12211 Research Triangle Park, NC 27709-2211				10. SPONSOR/MONITOR'S ACRONYM(S) ARO	
				11. SPONSOR/MONITOR'S REPORT NUMBER(S) 52606-PH.4	
12. DISTRIBUTION AVAILABILITY STATEMENT Approved for Public Release; Distribution Unlimited					
13. SUPPLEMENTARY NOTES The views, opinions and/or findings contained in this report are those of the author(s) and should not be construed as an official Department of the Army position, policy or decision, unless so designated by other documentation.					
14. ABSTRACT “Slow light” refers to the dramatic reduction in group velocity that can be obtained via a number of physical mechanisms. This project is focused on the fundamental principles of slow light in optical nanostructures and devices. Of particular importance is the use of slow light to enhance nonlinear optical processes, and the fundamental limitations thereof. The fundamental component of all slow light embodiments is a resonator, be it a micro-ring resonator, photonic crystal defect, or plasmonic resonant cavity. In addition to a new analysis					
15. SUBJECT TERMS slow light, nanophotonics, nonlinear optics					
16. SECURITY CLASSIFICATION OF:			17. LIMITATION OF ABSTRACT UU	15. NUMBER OF PAGES	19a. NAME OF RESPONSIBLE PERSON Steven Blair
a. REPORT UU	b. ABSTRACT UU	c. THIS PAGE UU			19b. TELEPHONE NUMBER 801-585-6157

Report Title

Enhanced nonlinear optical devices using artificial slow-light structures

ABSTRACT

“Slow light” refers to the dramatic reduction in group velocity that can be obtained via a number of physical mechanisms. This project is focused on the fundamental principles of slow light in optical nanostructures and devices. Of particular importance is the use of slow light to enhance nonlinear optical processes, and the fundamental limitations thereof. The fundamental component of all slow light embodiments is a resonator, be it a micro-ring resonator, photonic crystal defect, or plasmonic resonant cavity. In addition to a new analysis methodology, we have developed a new type of coupled-resonator slow-light waveguide that exhibits record delay bandwidth product per dB loss.

List of papers submitted or published that acknowledge ARO support during this reporting period. List the papers, including journal references, in the following categories:

(a) Papers published in peer-reviewed journals (N/A for none)

Liyong Diao and Steve Blair, "Optical bistability and multistability in 1-D photonic band gap structures," Journal of Optics A 9, 972-981 (2007)

Jeremy Goeckeritz and Steve Blair, "One-dimensional photonic crystal rib waveguides," Journal of Lightwave Technology 25, 2435-2439 (2007)

Tingjun Xu, Xiaojin Jiao, G.-P. Zhang, and Steve Blair, "Second-harmonic emission from sub-wavelength apertures: Effects of aperture symmetry and lattice arrangement," Optics Express 15, 13894-13906 (2007)

Vishnupriya Govindan and Steve Blair, "Nonlinear pulse interaction in microresonator slow-light waveguides," Journal of the Optical Society of America B 25, C23-C30 (2008)

Vishnupriya Govindan and Steve Blair, "Analysis of optical ARMA architectures in the slow-light regime," Journal of the Optical Society of America B 25, C116-C126 (2008)

Tingjun Xu, Xiaojin Jiao, and Steve Blair, "Third-harmonic generation from arrays of sub-wavelength metal apertures," Optics Express 17, 23582-23588 (2009)

Jeremy Goeckeritz and Steve Blair, "Optical characterization of coupled resonator slow-light rib waveguides," Optics Express 18, 18190-18199 (2010)

Number of Papers published in peer-reviewed journals: 7.00

(b) Papers published in non-peer-reviewed journals or in conference proceedings (N/A for none)

Number of Papers published in non peer-reviewed journals: 0.00

(c) Presentations

V. Govindan and S. Blair, “Limitations on nonlinear pulse propagation in coupled- resonator waveguides,” OSA Slow and Fast Light Topical Meeting, Salt Lake City, July 8-11, 2007.

J. Goeckeritz and S. Blair, “A one-dimensional photonic crystal rib waveguide,” OSA Slow and Fast Light Topical Meeting, Salt Lake City, July 8-11, 2007.

T. Xu and S. Blair, “Aperture symmetry and lattice arrangement modulated second- harmonic emission from sub-wavelength metallic apertures,” CLEO poster JWA15, San Jose, CA, May 7, 2008

(invited) S. Blair, “Nonlinear optics of sub-wavelength apertures,” 17th International Laser Physics Workshop, Modern Trends in Laser Physics presentation 1.2.2, Trondheim, Norway, June 30, 2008.

S. Blair, “Nanophotonics research activities,” SPIE Defense & Security 2010, Micro- and Nanotechnology Sensors, Systems, and Applications II, Orlando, FL, April 9, 2010.

Number of Presentations: 5.00

Non Peer-Reviewed Conference Proceeding publications (other than abstracts):	
V. Govindan and S. Blair, "Analysis of CROW, SCISSOR, and REMZI architectures in the slow-light regime," COTA/ICQI/IPNRA/SL on CD-ROM (The Optical Society, Washington, DC, 2008), STuB5.	
V.GovindanandS.Blair,"Four-wavemixinginslowlightwaveguides,"IPNRA/NLO/SL on CD-ROM (The Optical Society, Washington, DC, 2009), JWB3.	
J. Goeckeritz and S. Blair, "Slow light in coupled resonator large cross-section rib waveguides," in Integrated Photonics Research, Silicon and Nano Photonics (IPR)/Photonics in Switching (PS) (Optical Society of America, Washington, DC, 2010), IWC4	
Number of Non Peer-Reviewed Conference Proceeding publications (other than abstracts):	3

Peer-Reviewed Conference Proceeding publications (other than abstracts):	
X. Jiao, F. Mahdavi, J. Goeckeritz, S. Blair, H. Aouani, J. Wenger, M. Oldham, E. Devaux, and Th. W. Ebbesen, ``Influence of adhesion layers on the performance of plasmonic antennae," Fourth International Conference on Surface Plasmonic Photonics, Amsterdam June 21-26, 2009. (15% acceptance rate).	
Number of Peer-Reviewed Conference Proceeding publications (other than abstracts):	1

(d) Manuscripts	
Number of Manuscripts:	0.00

Patents Submitted	
-------------------	--

Patents Awarded	
-----------------	--

Graduate Students	
NAME	PERCENT SUPPORTED
Vishnupriya Govindan	1.00
Jeremy Goeckeritz	0.50
Tingjun Xu	0.50
FTE Equivalent:	2.00
Total Number:	3

Names of Post Doctorates	
NAME	PERCENT SUPPORTED
Xiaojin Jiao	0.50
FTE Equivalent:	0.50
Total Number:	1

Names of Faculty Supported		
NAME	PERCENT SUPPORTED	National Academy Member
Steve Blair	0.08	No
FTE Equivalent:	0.08	
Total Number:	1	

Names of Under Graduate students supported

<u>NAME</u>	<u>PERCENT SUPPORTED</u>
FTE Equivalent:	
Total Number:	

Student Metrics

This section only applies to graduating undergraduates supported by this agreement in this reporting period

The number of undergraduates funded by this agreement who graduated during this period:	0.00
The number of undergraduates funded by this agreement who graduated during this period with a degree in science, mathematics, engineering, or technology fields:.....	0.00
The number of undergraduates funded by your agreement who graduated during this period and will continue to pursue a graduate or Ph.D. degree in science, mathematics, engineering, or technology fields:.....	0.00
Number of graduating undergraduates who achieved a 3.5 GPA to 4.0 (4.0 max scale):.....	0.00
Number of graduating undergraduates funded by a DoD funded Center of Excellence grant for Education, Research and Engineering:.....	0.00
The number of undergraduates funded by your agreement who graduated during this period and intend to work for the Department of Defense	0.00
The number of undergraduates funded by your agreement who graduated during this period and will receive scholarships or fellowships for further studies in science, mathematics, engineering or technology fields:	0.00

Names of Personnel receiving masters degrees

<u>NAME</u>
Total Number:

Names of personnel receiving PHDs

<u>NAME</u>
Vishnupriya Govindan
Jeremy Goeckeritz
Total Number:

2

Names of other research staff

<u>NAME</u>	<u>PERCENT SUPPORTED</u>
FTE Equivalent:	
Total Number:	

Sub Contractors (DD882)

Inventions (DD882)

1 Overview

This report reviews our work over the past ~ 3 years on slow light nonlinear optics. Our work consists of three areas: 1) modeling studies on the performance limitations of slow light waveguides, 2) design, fabrication and characterization of a novel coupled-resonator slow light waveguide structure with low loss, and 3) experimental studies of harmonic generation processes in plasmonic nanostructures.

Of the most fundamental nature is our study of the limitations on the performance of slow light waveguides, both in the linear and nonlinear regimes. This work is based upon imposing a constraint on the amount of distortion that a pulse can experience upon propagation through a slow light waveguide. Much of this work has already been published (and reported previously), such as the effect of pulse distortion on the nonlinear phase shift, in that improvement in nonlinear sensitivity ceases after a certain number of resonators [1]. Another study showed how adjacent pulses interact in a nonlinear slow light waveguide [2], where certain slow light waveguide architectures (e.g. coupled-resonator optical waveguides, or CROW) suffer from relatively strong pulse to pulse interaction, and others (e.g. resonant-enhanced Mach-Zehnder interferometers, or REMZI) do not. We have also performed studies in the linear regime, comparing the three most common slow light waveguide architectures (CROW, REMZI, and side-coupled integrated sequence of spaced optical resonators, or SCISSOR) in terms of achievable bandwidth delay product in both the positive and negative (i.e. superluminal) group delay regimes [3]. The results of this study show that the REMZI architecture universally achieves the greatest bandwidth delay product. This is due to the greater degrees of freedom available in the REMZI structure. In section 2, an overview of our most recent work (to be completed) on the ultimate performance of slow light waveguides will be discussed, where the efficiencies of the three canonical architectures are compared to each other and to the ultimate performance predicted by digital filter optimization.

We have also been working on fabricating a novel photonic crystal based slow light waveguide structure in silicon for use in nonlinear optical studies. The novel design reduces the out of plane scattering loss that virtually all other designs suffer from. This loss mechanism is exacerbated in high index contrast materials systems, leading to a tradeoff between bandwidth delay product and loss. Our design uses relatively large cross-section single mode rib waveguides and deep trench etching to simultaneously achieve high index contrast and very low loss, as originally proposed in [4]. We have developed some new nanofabrication methods in order to realize this structure, which, along with characterization results [5], are discussed in section 3.

Finally, we have been investigating “slow light” effects on the nanoscale. In particular, we have been interested in very small apertures in metal films, which serve as tiny cylindrical waveguides, and other optical “antennae.” When operating these waveguide just below the cutoff wavelength for the TEM_{00} mode, the optical density of states increases, leading to significantly reduced group velocity [6] and enhanced intensity [7]. We have been exploiting this effect for nonlinear optical processes such as second-harmonic generation [8] and third-harmonic generation [9]. These results are overviewed in section 4.

2 Performance limitations of slow light waveguides

Ever since the demonstration of dramatic reduction in the group velocity of light [10], there has been growing interest in the physics and applications of slow light. One of the more flexible implementations of slow light is via coupled optical microresonators [11, 12, 13, 14] (note that related structures in the microwave regime have been studied since the 1960's [15, 16]). A particular application of interest for slow-light structures lies in fixed and tunable optical delay lines [17, 18, 19, 20]. The “length” of a delay line is often characterized by the number of pulse delays [21], a metric which is related to the bandwidth-delay product.

One of the important questions in the design of slow-light waveguide structures is the maximum achievable number of pulse delays. While in the absence of loss, a long-enough structure could always be designed to meet a given criterion, a more interesting question is the ultimate efficiency of a structure, such as measured by the number of pulse delays per resonator. This efficiency metric is highly architecture and design-dependent (this metric also depends strongly on pulse shape [3]). We have taken the general approach of discrete time filters [22, 23], where filter design is first performed in the digital domain and mapped to an optical architecture. Discrete-time filter design concepts [24] have been widely used to analyze optical filter configurations, primarily in terms of their linear response. One of the limitations of this approach is that designs cannot always be efficiently mapped, and often, some constraints are imposed on the optical design.

The aim of this work is to compare the performance of filters in the digital and optical domains under the constraint of fixed pulse distortion. The performance measure for these filters is the number of pulse delays that can be achieved, which is defined as the ratio of the group delay to the incident pulse duration. Both AR (all-pole) and ARMA (pole-zero) designs are studied. The corresponding optical architecture to the AR digital filter is the coupled resonator optical waveguide or CROW. The corresponding optical architectures to ARMA digital filters are side coupled integrated spaced sequence of resonators (SCISSOR) and ring enhanced Mach-Zehnder interferometer (REMZI). The performance (number of pulse delays) obtained with digital filters is better than the optical filters because all the degrees of freedom for optical filter design are typically not utilized. Often, the ring length is a fixed value in order to simplify the mapping and/or optimization procedure, but that constraint results in reduced number of pulse delays. We delve into this issue further by demonstrating the improvement obtained by including the ring length in a direct optimization method. However, due to the increased number of free parameters to optimize with for a higher number of stages, efficiency (number of pulse delays per resonator) can drop. The digital and optical architectures of AR and ARMA filters are presented in section 2.1. In section 2.2, design and optimization methods for both digital and optical filters are discussed. In section 2.3, the number of pulse delays for AR filters is studied, and in section 2.4, results for ARMA designs are presented.

2.1 AR and ARMA filters architectures

The optical filter architectures and their transfer matrices are discussed in this section. In general, there are two classes of digital filters - finite-impulse response (FIR) and infinite-impulse response (IIR). We will focus on IIR-type filters, which are characterized by poles in their transfer functions, and can be associated to optical resonances. The basic IIR filter consists of all-poles (but may have zeros at the origin) and is termed autoregressive (AR), while an IIR filter that contains zeros outside the origin is autoregressive moving average (ARMA). In general, ARMA filters have an advantage of tailoring the phase response by altering the locations of the zeros which can be useful for applications like dispersion compensation and linearized phase modulation.

Figure 1 shows the generic CROW architecture [11] which consists of a sequence of N directly-coupled microring resonators. Each ring has a physical length, or circumference, L , with free spectral range $FSR = c/nL$, where $n = 3.0$ is the assumed effective refractive index (Si), and a slow-light waveguide consists of N such coupled resonators. The coupling coefficients are denoted by σ_i , where i indexes the coupling regions, numbering from 1 to $N+1$. We assume that all couplers are ideal, i.e., no coupling loss and no backward reflection, so that operation is solely determined by the field coupling coefficients τ and σ that are related by $\tau^2 + \sigma^2 = 1$. The corresponding digital filter consists of \sqrt{N} zeros at the origin and N independent poles, which is termed an AR lattice filter.

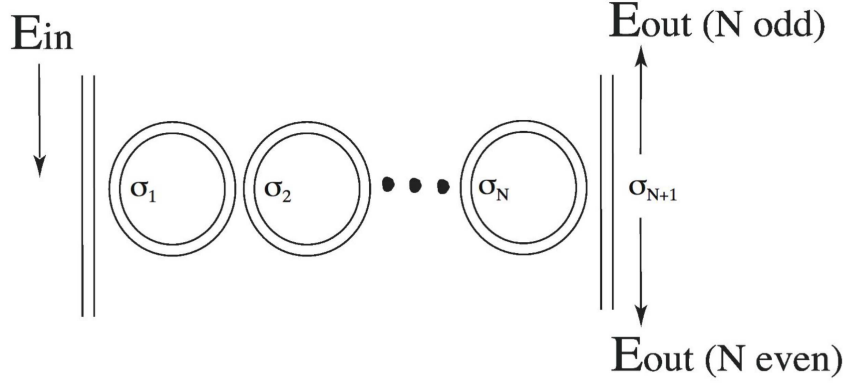


Figure 1: CROW architecture

Figure 2 illustrates a sequence of waveguide-coupled resonators, forming a SCISSOR [13,14]. The unit cell transfer function for the SCISSOR architecture is given by the equation

$$H_{ring} = \frac{E_{out}}{E_{in}} = \frac{\tau - e^{j\phi}}{1 - \tau e^{j\phi}}, \quad (1)$$

where $\phi = kL$ and $k = 2n\pi/\lambda$. The transfer function possesses one pole ($p1 = 1/r$) dependent on its zero ($z1 = r$), and is a constrained ARMA filter. For N resonators, the transfer function is simply H_{ring}^N .

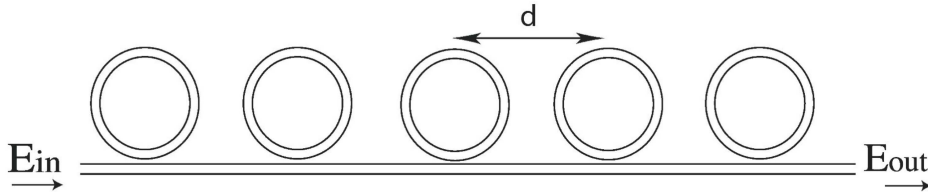


Figure 2: SCISSOR architecture (top) and unit cell (bottom).

The architecture of the REMZI filter with a single ring is shown in Fig. 3, where k_i represents the MZI coupling coefficients and ϕ_R and ϕ_{mzi} are the phase shifts in the ring and MZI respectively.

The output of the unit cell is expressed by the following transfer matrix relation:

$$\begin{bmatrix} E_{out1} \\ E_{out2} \end{bmatrix} = \Phi \begin{bmatrix} E_{in1} \\ E_{in2} \end{bmatrix} \quad \text{where} \quad \Phi = \begin{bmatrix} H_{ring} & 0 \\ 0 & e^{-j\phi_{mzi}} \end{bmatrix} \times \begin{bmatrix} \sqrt{1-k_i^2} & jk_i \\ jk_i & \sqrt{1-k_i^2} \end{bmatrix}. \quad (2)$$

In the above equation, H_{ring} is the transfer function of the ring-waveguide configuration given by equation 1. For N stages, the corresponding digital filter consists of N zeros and N poles which are independent of each other; this architecture is represented by an ARMA lattice filter. The independent zeros of the REMZI architecture can be used to engineer its phase response [25, 22].

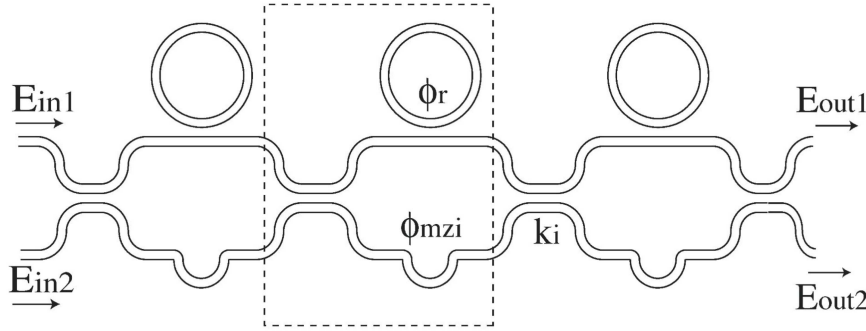


Figure 3: REMZI architecture

2.2 Filter design and optimization

This section presents the design and optimization methodologies we have developed over the course of our research for digital and optical filters. Two methods are studied to maximize the group delay under the constraint of fixed output pulse distortion. The first method is called the bandwidth tuning method, where a prototype linear frequency response is selected for the optical filter. Next, the optical architecture is analyzed using the z-transform [26]. Then, an optimized discrete filter is designed to give the same frequency response as the prototype response desired from the optical architecture. Next, a mapping algorithm [27] is derived to synthesize the parameters of the optical architecture from the discrete filter. The synthesized optical filter is then simulated using electromagnetic models and its linear response is verified to be the same as that of the discrete filter. The bandwidth of the prototype filter is tuned in order to obtain 5% output pulse distortion. The mapping algorithm between the digital and optical domains has limitations that prevent achieving the desired filter characteristics with the optical architecture. Hence, the group delay of the optical architecture obtained from the bandwidth tuning method is lower than that of the prototype digital filter.

The second method, called the direct optimization method, involves optimizing the filter coefficients directly in the digital and optical domains. In the digital domain, the position of the poles (AR, ARMA) and zeros (ARMA) are directly tuned to maximize the group delay under the constraint of 5% output pulse distortion. In the optical domain, the coupling coefficients and phase shifts of the optical architecture are tuned to maximize the group delay under the same distortion constraint. This method gives higher group delay in both domains for the same distortion constraint due to more degrees of freedom. In addition, direct optimization narrows the performance gap between the digital and optical designs.

Pulse distortion is calculated based on the following equation [1]:

$$D = 1 - \frac{\int_{-\infty}^{\infty} |E_{in}(t - t_{gd}) E_{out}^*(t)| dt}{\int_{-\infty}^{\infty} |E_{in}(t)|^2 dt} \quad (3)$$

where t_{gd} is the average group delay of the optical architecture and is calculated based on the first moment of the output pulse intensity as given by

$$t_{gd} = \frac{\int_{-\infty}^{\infty} t |E_{out}|^2 dt}{\int_{-\infty}^{\infty} |E_{out}(t)|^2 dt}. \quad (4)$$

The group delay is maximized for a 10 ps input pulse duration.

2.3 Analysis of AR digital and optical filters

This section discusses the design and evaluation of optical AR lattice filters using the digital filter design approach and compares the performance of AR filters in the digital and optical domains.

We first look at the digital AR lattice filter. Figure 2.3 plots the number of pulse delays for the two optimization methods. It should be noted that with the bandwidth tuning method, the prototype filter response is maximally flat with unit magnitude over the design bandwidth. The design from the bandwidth tuning method is used as the starting point for direct optimization. It is clear that direct optimization produces a significant increase in efficiency, approaching 0.5 pulse delays/stage.

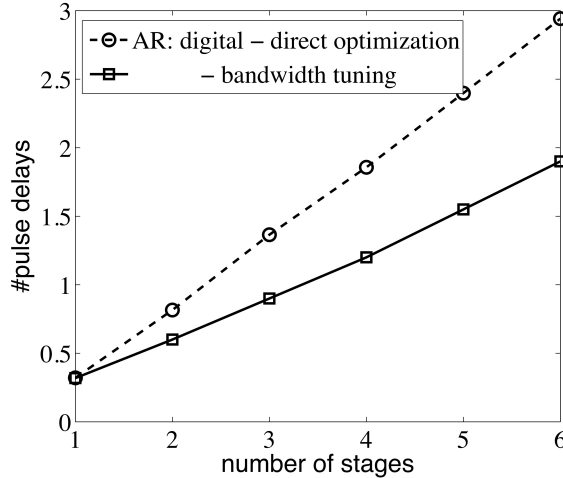


Figure 4: Number of pulse delays in the digital domain (AR) versus number of stages constrained by 5% output pulse distortion. Digital designs from direct optimization and bandwidth tuning methods.

In order to implement the bandwidth tuning method for CROW, we use a procedure developed by Melloni [28], where a prototype filter is synthesized using a classic microwave filter design and then substituted with optical components, such as coupled ring resonators. Direct optimization is then based upon using this design as an initial guess. The second design method shows an increase in the number of pulse delays per stage, as shown in Figure 5. It should be noted that the mapping algorithm is not efficient for arbitrary pole locations and when the poles get close to the unit circle, thus, failing to preserve the digital filter characteristics in the optical domain.

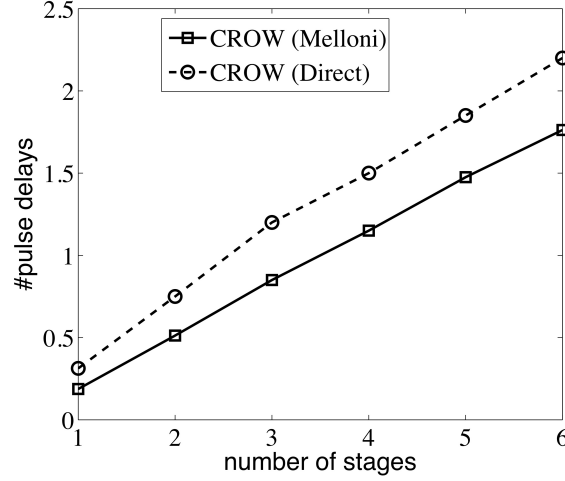


Figure 5: Number of pulse delays (AR) versus number of stages for optical designs with 5% output pulse distortion from direct optimization and bandwidth tuning methods.

In order to compare the direct optimization designs in the digital and optical domains, the number of pulse delays is plotted versus the number of stages in Figure 6. The discrepancy in the number of pulse delays between the two domains increases for higher number of stages. This is mainly due to the fact that all of the degrees of freedom are not used in the optimization for the CROW designs. The additional degree of freedom is the ring length. By including variable ring length in the direct optimization, the performance of the optical design nearly matches that of the digital design.

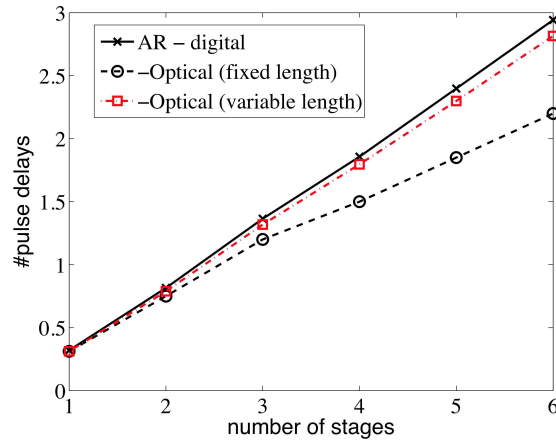


Figure 6: Number of pulse delays (AR) versus number of stages with 5% output pulse distortion. Digital and optical designs from the direct optimization method.

2.4 Analysis of ARMA digital and optical filters

ARMA architectures have poles and zeros, increasing their design flexibility. In general, the performance of ARMA filters in the digital and optical domains is better than that of AR designs.

We again use the two design methods for the ARMA filters. In the first method, we tune the filter bandwidth which moves the pole-zero locations in the digital domain, and in turn determines the coupling coefficients in the optical domain. The number of pulse delays is plotted in Figure 2.4 for the bandwidth tuning method. For $N = 1$, SCISSOR and REMZI designs have the same group delay for 5% pulse distortion as a single stage of REMZI reduces to a single waveguide coupled resonator.

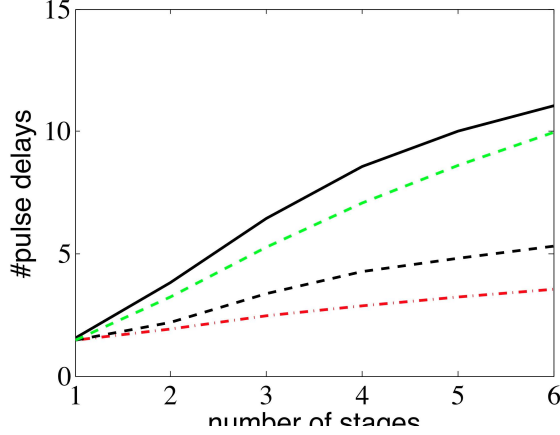


Figure 7: Number of pulse delays (ARMA) versus number of stages. 5% output pulse distortion. Digital and optical designs from direct optimization method.

With the direct optimization method, the design from the bandwidth tuning method is used as a starting point for subsequent optimization. In the digital domain, direct optimization of the locations of the poles and zeros is performed to maximize the group delay under the same 5% distortion constraint. For the optical architectures, the coupling coefficients (SCISSOR and REMZI) and phase shifts (REMZI) are directly optimized. Similar to the AR designs, the direct optimization method results in improved ARMA designs. In Figure 2.4, we plot the number of pulse delays for both digital and optical designs obtained from the direct optimization method. The results for REMZI are plotted for both fixed and variable ring lengths. Variable ring length results are not plotted for SCISSOR as it did not produce any significant improvement. It can be observed that, by including ring length in optimization, the performance improves and gets closer to digital domain. However, there is still discrepancy due to the difficulty in optimization for higher number of stages due to increased free parameters to optimize with.

The transfer function for digital design with $N = 3$ is presented in Figure 8 for 5% output pulse distortion level under direct optimization. The transfer functions for the optical ARMA designs for $N = 3$ are presented in Figure 9 (REMZI and SCISSOR) along with the corresponding pole zero diagrams. The output pulse profiles for the ARMA designs is presented in Fig. 11

2.5 Conclusion

Digital filter design concepts were applied to study the limits on the performance of slow-light optical filters in terms of the number of attainable pulse delays per stage, as well as in numerous other studies based upon nonlinear pulse propagation. Traditional design methods based upon prototype digital filters do not produce optimal performance in either domain, and there are discrepancies between the two domains due mainly to limitations/constraints in the procedure that maps poles and zeros into optical coupling and phase shift coefficients. However, direct optimization improved the filter

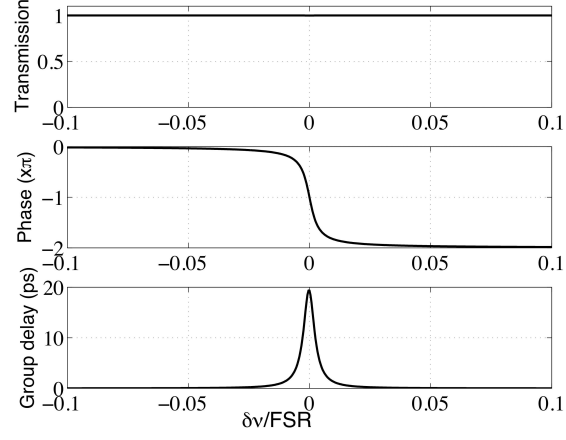


Figure 8: Transfer function for the digital ARMA filter under direct optimization - $N = 3$ and 5% output pulse distortion.

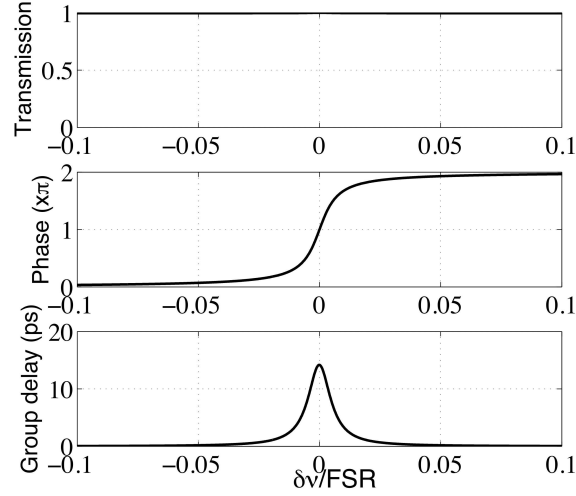


Figure 9: Transfer functions (top) and pole zero diagrams (bottom) for the REMZI and SCISSOR optical architectures under direct optimization - $N = 1$ and 5% output pulse distortion.

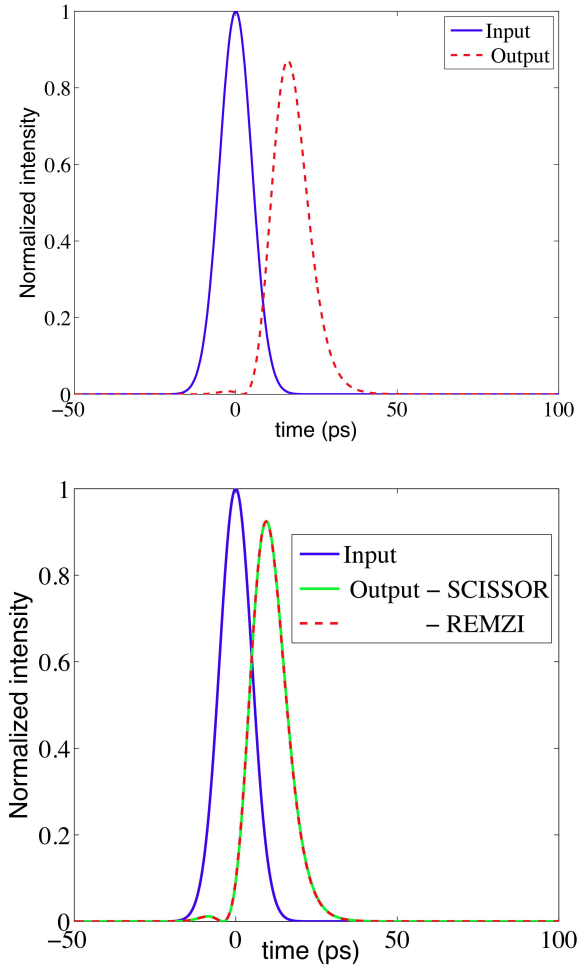


Figure 10: Output pulse profiles for the ARMA designs under direct optimization. Digital (top) and optical (SCISSOR and REMZI, bottom) with $N = 1$ and 5% pulse distortion.

performance in both domains. We showed that the primary cause of the discrepancy between digital and optical designs is due to constraining the optical designs to a fixed ring length. When the ring length was also included as a free parameter in optimization, the performance improved and became closer to the corresponding digital filter designs. From our results, we estimate that the CROW optical architecture can produce 0.5 pulse delays/stage, while SCISSOR and REMZI produce 0.7 and 1.5, respectively.

Our work has consistently demonstrated that the REMZI slow-light architecture is the most efficient across all metrics related to linear and nonlinear effects. However, REMZI architectures are the most difficult to fabricate.

3 Low loss photonic crystal slow light waveguides

We have completed the fabrication and testing of the photonic crystal rib waveguide design. The nature of the design significantly reduces out of plane scattering (which occurs via diffraction from unguided regions of the photonic crystal) by using a large cross-section rib waveguide for transverse confinement, which supports single mode operation with large mode size. The major disadvantage of this approach is that, in order to etch air gaps, or trenches, into the rib waveguide to define the photonic crystal in the longitudinal direction, high-aspect ratio etching is required. As shown in Figure 11, the thickness of the Si layer is $5.3\text{ }\mu\text{m}$. For a quarter-wave length air spaced mirror period, the width of the etched trench must be $\sim 330\text{ nm}$ at 1550 nm operating wavelength, requiring an aspect ratio of 16:1 or greater.

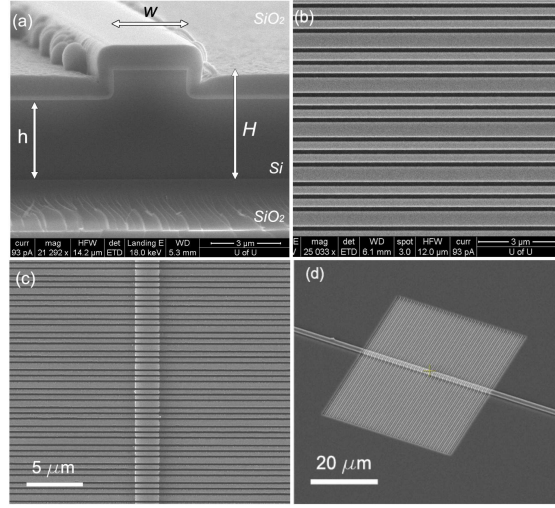


Figure 11: Micrographs of the slow light waveguide. a) Cross-section of a rib waveguide showing the top and bottom SiO_2 claddings. The rib waveguide has a height of $H = 5.3\text{ }\mu\text{m}$, a rib width of $w = 3.8\text{ }\mu\text{m}$, and a slab height h . b) A magnified view of the surface of the high aspect ratio trenches. Three trenches are used to separate each resonator. c) The trenches shown are etched through the rib waveguide. d) A structure with 25 coupled resonators. The input and output rib waveguides can be seen leading to the CROW.

The slow-light waveguides are fabricated on a 100 mm SOI wafer using a series of surface micromachining processes. The flow diagram for the fabrication is shown in Figure 12. The first fabrication step is to perform optical lithography to create alignment marks for the trenches and waveguides. The alignment marks are etched into the wafer using reactive ion etching (RIE) with SF_6 and O_2 gases. Next, a thin layer of Cr is sputtered over the wafer followed by a spin-on layer of resist (ZEP 520A, Zeon Corp.). The resist is patterned using e-beam lithography (NovaNano, FEI) and then developed. The pattern is transferred to the Cr using RIE with Cl_2 gas. The Si is then patterned using cryogenic deep reactive ion etching (DRIE) using SF_6 and O_2 gases. The etch recipe gives smooth vertical sidewalls. The residual Cr mask is removed using wet etching (Cr-14 etchant).

Next, the rib waveguide is formed over the trenches using optical lithography and another DRIE step. This etching step uses a much higher pressure than the previous DRIE step to create a short mean free path between reactive gas molecules which prevents etching at the bottom of the trenches. The waveguide must be aligned perpendicularly to the trenches to avoid deflecting light

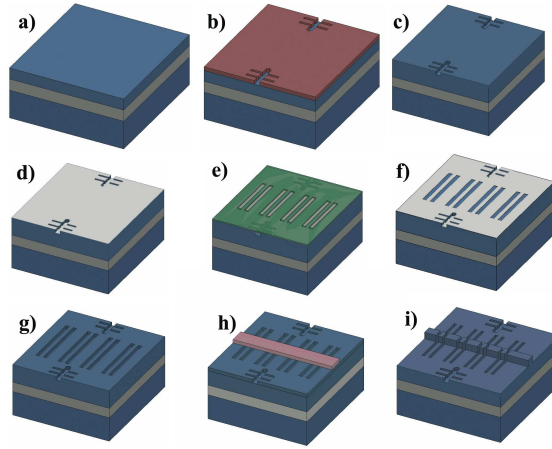


Figure 12: Process steps used to fabricate the waveguides. a) An SOI wafer is processed starting with b) an optical lithography step using a positive photoresist (Shipley 1813) and c) dry etching using RIE. d) A layer of Cr is sputtered on the wafer surface followed by e) a spin-on layer of e-beam resist. The resist is then patterned and f) the Cr is etched using RIE. The Cr mask is then used as a mask during g) etching of the trenches. h) Another optical lithography step is used to create an etch mask for the rib waveguide, which is i) etched using a short DRIE step.

out of the waveguide. The alignment is better than a half degree from 90° , similar to state-of-the-art fabrication quality achieved by others.

The trenches are back filled by wet oxidation. The wet oxidation is self-arresting as the oxide from both sides of the trenches meet. The purpose of the oxidation is to reduce surface roughness inside the trenches which lowers the waveguide loss. Roughness scattering is particularly detrimental to slow light waveguides because the scattering loss scales with the square of the electric field.

We've achieved high aspect ratio etching using an inductively coupled plasma (ICP) reactive ion etching (RIE) system. Examples of this high aspect ratio etching are shown in Figure 13. Two types of structures have been made. The first is with the photonic crystal region defined by air gaps. In order to obtain the advantages of reduced out of plane scattering, vertical symmetry should be maintained, which is achieved by using chemical vapor deposition (PECVD) of an oxide cladding layer. While there is some deposition into the air trenches (seen by tapering of the top portions of the trenches), the air trenches remain intact. The other structure has trenches filled in with oxide, which is accomplished by wet thermal oxidation of the structure after the air trenches have been etched. This requires compensation of the initial trench width due to the take-up of Si material during oxidation; PECVD oxide is then deposited as a top cladding layer to maintain symmetry.

Transmission measurements through these PCRWs have been made using a tunable telecom laser. The transmission spectra are then normalized to the transmission measurement through identical rib waveguides (but without the PC structure). Some of the results are shown in Figure 14 for structures with 5, 10, and 25 resonators. A few features can be noticed from these results. In general, the entire bandgap of the structures is wider than the tuning range of our laser (approximately 180 nm), where only the high frequency bandedge and central defect transmission resonance are within range; the entire bandgap region is expected to cover approximately 200 nm, corresponding to 13% fractional bandwidth (for an air trench structure, the width will be even greater). Another feature is the large dynamic range between the transmission windows and the bandgap region, exceeding 10^3 for 25 resonators. The number of peaks in the miniband corresponds

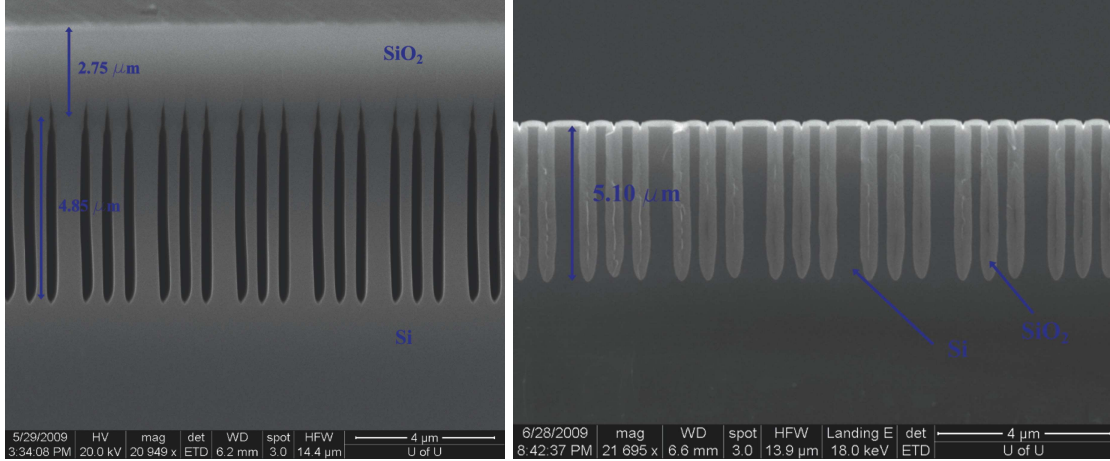


Figure 13: Cross-section images of the photonic crystal region of PCRWs using an SiO₂ cover layer with air trenches (left) or using wet oxidation to fill-in the trenches (right).

to the number of resonators; as the number of resonators increases, the transmission band becomes flatter with sharper roll-off, as expected for $N \rightarrow \infty$. Finally, what is most surprising is the high transmission through the PCRW, where up to 70% transmission is obtained through 25 resonators.

We have calculated the slowing ratio and propagation losses for these structures. The slowing ratio is 29 and the loss is just under 1.5 dB/cm, where the effective path length has been used. For slow light waveguides to be used in all-optical networks as time-delay buffers, they must be capable of significantly reducing the group velocity. In addition, they must also have a wide bandwidth to accommodate optical signals and avoid pulse distortion. Therefore, the delay-bandwidth product (DBP) is an important figure of merit. For the 25 resonator waveguide, the bandwidth over which n_g varies by $\pm 10\%$ about the average n_g is 16 nm. The calculated delay time is 5.4 ps, giving a DBP of 10.8. This is a relatively large value and compares well to state-of-the-art slow light waveguides (see Table 1).

The DBP could be increased by coupling more resonators together. However, as more cavities are added, loss also increases, limiting the practical length. Therefore another important figure of merit is the DBP per unit loss. For our structure with 25 resonators the DBP/loss is 38 per dB, which is also shown in Table 1 along with the values for several other slow light waveguides from the literature. On a DBP/loss basis, the waveguide presented here essentially ties for best performance. The normalized DBP (nDBP) is also an important figure of merit for comparing the performance of various waveguides. The nDBP is defined at $n_g(\Delta\omega/\omega)$, where ω is the frequency and $\Delta\omega$ the bandwidth. For the structure presented here, the value is 0.31, which is higher than any other slow light structure.

Despite the relatively large height of the rib waveguide, the overall footprint of the structure is still quite small. The 25 resonator CROW as fabricated occupies a surface area of approximately $3 \times 10^{-3} \text{ mm}^2$, which is nearly half the footprint of 25 coupled ring resonators, assuming 8 μm radii and 200 nm gaps. The rib waveguide CROW footprint could be reduced further by shortening the length of the trenches. Our BPM simulations show that the trenches only need to be 6 times the waveguides rib width w . Therefore, the footprint of the 25 resonator structure could be reduced to $1.4 \times 10^{-3} \text{ mm}^2$. This compact footprint makes the rib waveguide CROW promising for on-chip integration with other optical structures.

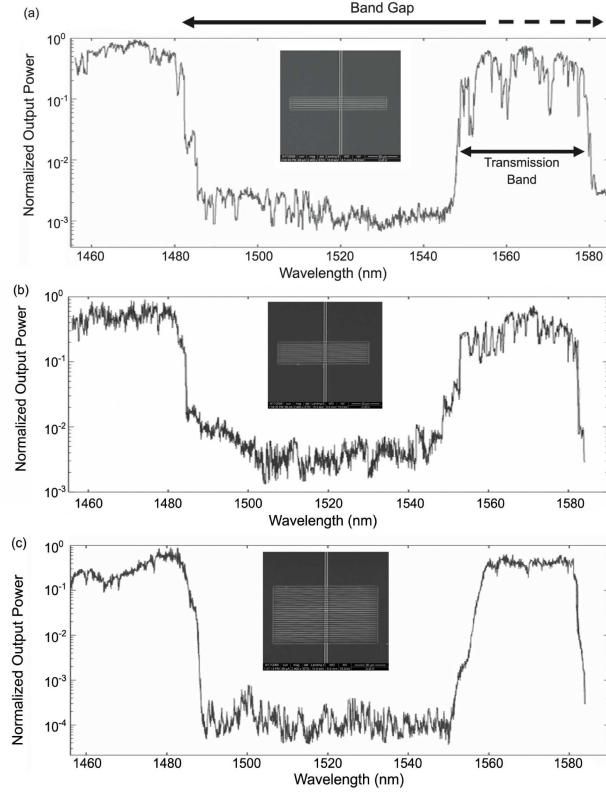


Figure 14: Normalized transmission measurements through PCRWs of 5 (top), 10 (middle) and 25 (bottom) defect resonators.

Table 1. Comparison of slow light waveguides from the literature.

Structure	Measurement Type	Group Index	DBP	Propagation Loss (dB/cm)	DBP/loss (dB ⁻¹)	Reference
1. Coupled Rib Waveguide Resonators ^a	Spectral	30.1	10.8	52.7	38.0	Presented Here
2. Coupled PC Resonators	Temporal and Spectral	129	11.0 ^b	14.5 ^c	39.9	Notomi [10]
3. Coupled PC Resonators	Spectral	105	3.0 ^d	3x10 ³	0.4	Jágerská [28]
4. Coupled Ring Resonators	Temporal and Spectral	36.3 ^e	55 ^e	126 ^e	2.4	Xia [9]
5. PC Band Edge	Spectral	34	78 ^f	150	10.4	Frandsen [30]
6. PC Band Edge	Spectral	25	30	244	7.7	Settle [31]
7. PC Band Edge	Spectral	42	57	-	-	Baba [32]
8. PC Band Edge	Spectral	44	15.8 ^d	-	-	Li [29]

^a Measured for a 25 resonator structure with the n_g spectrum shown in Fig. 6.

^b Calculated using bandwidth of 1.2 nm, $N = 60$ resonators, $v_g = 7.7 \times 10^{-3}c$, and 75 ps delay time.

^c Estimated loss.

^d Calculated from paper.

^e Calculated for 100 coupled rings in CROW configuration, i.e. 9 μm radii and 200 nm gap. The linear length is used to calculate the propagation loss and group index, not the total path length. A 2 nm bandwidth centered at 1550 nm is used to calculate DBP.

^f Calculated with 11 nm bandwidth, i.e. bandwidth over which n_g is reported to be constant.

Figure 15: Comparison of slow light waveguides from the literature. The citations can be found in the Optics Express 2010 paper.

4 Third harmonic generation from sub-wavelength apertures

Extraordinary optical transmission (EOT) through metal films modulated with a 2-D array of sub-wavelength apertures [29] was reported in 1998. It is now well established that upon the condition of EOT, intensity buildup within the apertures can occur [30, 31], motivating the study of nonlinear processes. Indeed, resonant enhancement of second-harmonic generation (SHG) by a factor of 10^4 has been demonstrated for a single sub-wavelength aperture surrounded by periodic annular corrugation [32]. SHG has also been studied in arrays of sub-wavelength apertures of various shapes, using disordered [33, 34, 8] and periodic [34, 35, 36, 37, 38] arrangements. The effect of the symmetry of the aperture has been shown [34], in that, at normal incidence, apertures with inversion symmetry produce much weaker SH than non-centrosymmetric apertures, while at off-normal incidence, SH can be produced with centrosymmetric apertures [34, 38, 8].

So far, nonlinear optical studies have been directed towards $\chi^{(2)}$ effects, although multi-photon luminescence has been observed [37]. Closely related are nonlinear optical studies using bow-tie antennae, where strong field enhancement is obtained within the feedgap [39]. Recently, high-harmonic generation was demonstrated utilizing the strong field enhancement within the gaps of bow-tie antennae [40]. Our focus is on third-harmonic generation (THG) in transmission from sub-wavelength metallic apertures arrayed in gold films, where the effects of aperture size and spacing on conversion are demonstrated.

4.1 Experimental methods

Arrangements of sub-wavelength apertures were produced in 100 nm thick gold films using electron beam lithography (EBL). Briefly, a 5 nm chromium or TiO_2 adhesion layer was sputter deposited onto the quartz substrate, followed by 100 nm of gold and 20 nm of chromium. ZEP520A e-beam resist of about 300 nm thickness was spin coated. Following e-beam exposure, the upper chromium layer was dry etched with chlorine, and the e-beam resist removed. The chromium layer served as a hard mask for argon ion milling of the gold. A wet etch removed the upper chromium layer (and likely resulted in some undercut in the underlying chromium adhesion layer). For samples with TiO_2 as the adhesion layer, we used reactive sputtering to produce the ~ 5 nm TiO_2 layer by introducing O_2 during the sputtering process; pure O_2 was flowed through the chamber to fully oxidize the thin film before the chamber was pumped down to sputter the gold film.

The experimental setup is similar to the one used previously [8], as shown in Fig. 16. A Ti:Sapphire laser is used at 800 nm wavelength and roughly 30 fs pulse duration. The setup allows the rotation of the sample with respect to the incident fundamental beam as well as rotation of the detector around the sample so that the radiation pattern can be measured in transmission. The detector is a blue-sensitized PMT (H5784-03) and two spectral filters are used to block the transmitted fundamental at 800 nm and minimize the influence of broadband background luminescence [37]. The angular acceptance of light collection is roughly 1 degree through a slit of about 2 mm width. Lock-in detection is performed by modulating the 86 MHz pulse train at 2 kHz, and average incident power is 75 mW (measured after the chopper), except where noted.

4.2 Results

One significant difference between SHG and THG is that THG does not have the symmetry limitations of SHG. This can be seen in Fig. 17 which plots the fundamental transmission, SH output, and TH output versus incidence angle for a sample with Cr adhesion layer, and 885 nm spacing of round holes. Because of centro-symmetry of the sample at normal incidence, there can be no

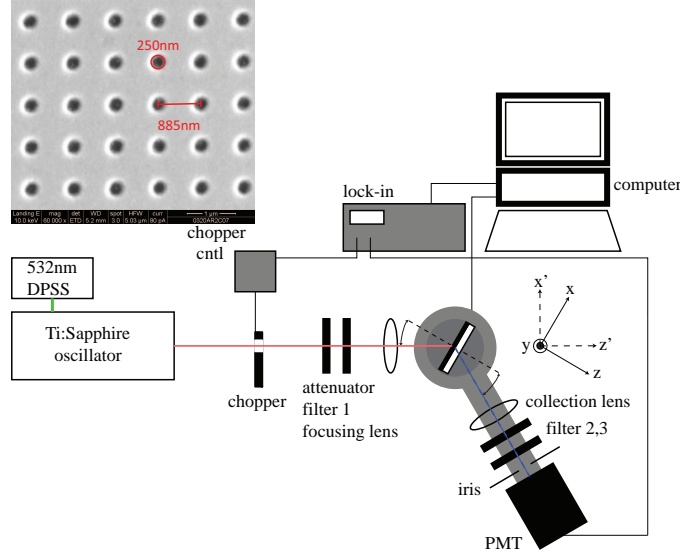


Figure 16: Experimental setup for third harmonic generation measurements. The output of the Ti:Sapphire laser passes through a neutral density filter and a spectral longpass filter (690 nm) before being focused onto the sample with a $20\text{ }\mu\text{m}$ spot size by a 10 cm focal length lens; all patterned areas were larger than the spot size (EBL samples are $80\text{ }\mu\text{m}$ by $80\text{ }\mu\text{m}$). Emission from the sample passes through a collection lens of 5 cm focal length made from fused silica, a spectral UG5 glass filter (Thorlabs) with passband around 225 nm to 400 nm to suppress the fundamental, an Hg line interference filter (CVI, 265 nm center, 25 nm passband) to isolate the TH, and a 2 mm slit, and is detected with the PMT.

SH output [34, 8]. However, the $\chi^{(3)}$ response always exists. As shown in Fig. 17, the TH output peaks with maxima in fundamental transmission, indicating that the greatest intensity enhancement within the aperture occurs at the transmission maxima, as expected.

Power scaling of the SH and TH signals are also shown in Fig. 17. The measured data points are plotted on a log-log scale and fit to a linear equation with slopes of 2.0 and 2.8, respectively, for SH and TH, which represent the power scaling factors. From the measurements, it is clear that the samples can withstand average incident power levels where the TH signal is about the same as the maximum SH (under strong symmetry-breaking conditions), not correcting for differences in collection efficiencies and PMT responsivity. Whether this holds for even higher harmonics is not known yet.

Double-angle scans for SHG and THG using the sample with Cr adhesion layer are shown in Fig. 18, where both the incidence and detection angles are varied. Again, the difference between the SHG and THG mechanisms is observed in that there is minimal SH under conditions of inversion symmetry (normal incidence and normal detection), other than a small two-photon luminescence background. The peaks in the detection scan correspond to coherent emissions from the apertures that satisfy the following momentum matching condition [8]:

$$\mathbf{k}_t^{n\omega} = n\mathbf{k}_t^\omega + m\mathbf{K}, \quad (5)$$

where n is the harmonic order, \mathbf{K} is a reciprocal lattice vector with $|\mathbf{K}| = 2\pi/\Lambda$, Λ is the aperture spacing, m is the diffraction order, and \mathbf{k}_t represents a transverse light wave-vector. For a square lattice, and assuming that the optical wavevectors have only the \hat{x} transverse component (since the

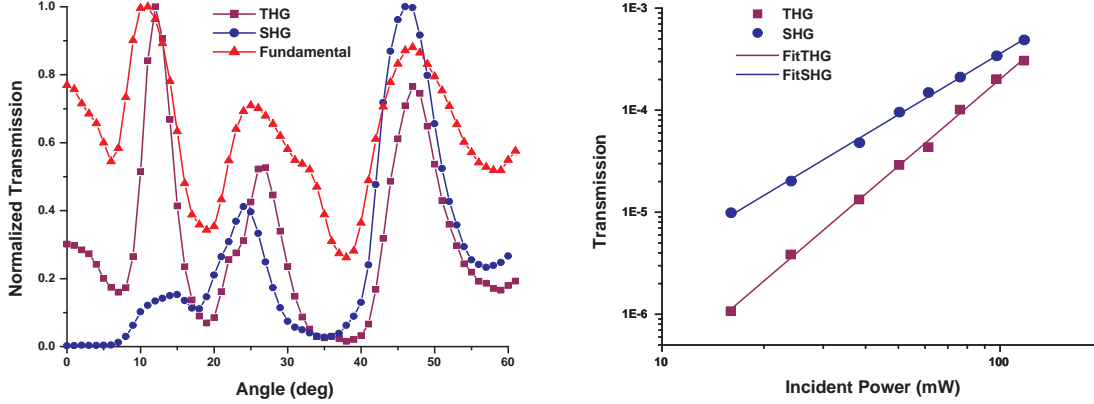


Figure 17: Fundamental transmission, second-harmonic output, and third-harmonic output versus incidence angle for a sample of 200 nm holes with 885 nm spacing in a square lattice (left). The adhesion layer is 5 nm of Cr. Power scaling of second-harmonic and third-harmonic outputs (right). For THG measurement, the sample was set for a 12° incidence angle, while for SHG measurement, the sample was set for 46° incidence.

scans are performed along only one axis), this equation can be written

$$\sin \gamma = \sin \theta + m \frac{\lambda}{n\Lambda}, \quad (6)$$

where γ is the detection angle and θ is the incidence angle. Therefore, the angular spacing between peaks in the TH measurements are narrower due to the shorter wavelength of emission ($n = 3$). At detection angles that lie in-between these peaks, luminescence background can be observed. Since two- and three-photon luminescence are incoherent emissions, they produce broad angular spectra, which is clearly evident. Evidence that the luminescence emits from the apertures is given by the fact that the luminescence is strongest at the same incidence angles that the SH and TH peaks occur.

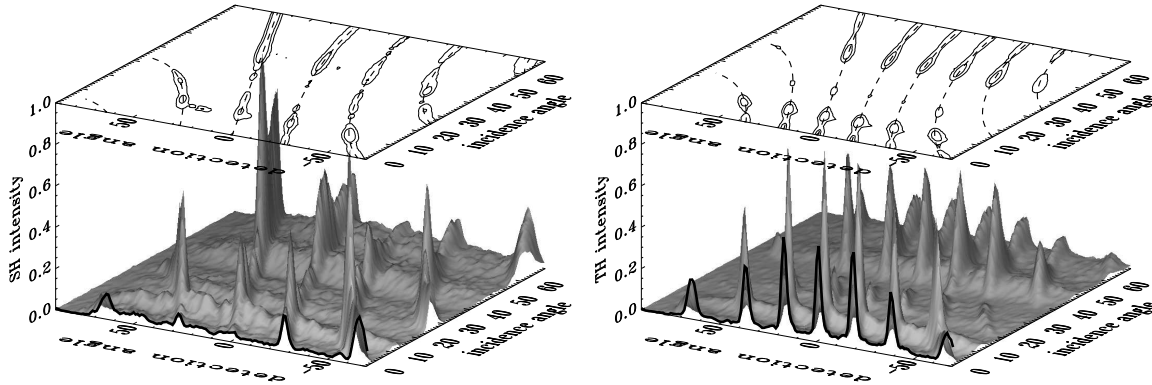


Figure 18: SH (left) and TH (right) emission for a sample with Cr adhesion layer, 885 nm pitch, and 200 nm aperture diameter. The SH and TH signal intensities are normalized to the same value. Trajectories of the diffraction peaks follow equation 6, as indicated by the dashed lines on the contour plots.

A practical issue not always addressed for plasmonic structures is the adhesion layer. Often-

times, a thin layer of Cr is used to promote the adhesion of Au to a glass substrate. However, Cr is a highly lossy material, and can cause significant attenuation of SPP propagation at the metal/substrate interface [41, 42]. We performed all subsequent TH measurements on samples with TiO₂ adhesion layers. The effects of different adhesion layers will be discussed in a separate paper.

4.2.1 Effects of aperture spacing

Keeping the aperture size fixed at 250 nm, we investigated the effects of varying the spacing. The results are shown in Figure 19 for both the transmission of the fundamental beam and emission at the TH wavelength. In these measurements, the sample was rotated with respect to the incident beam (varying θ) and detection was performed at the zeroth order transmission ($\gamma = -\theta$).

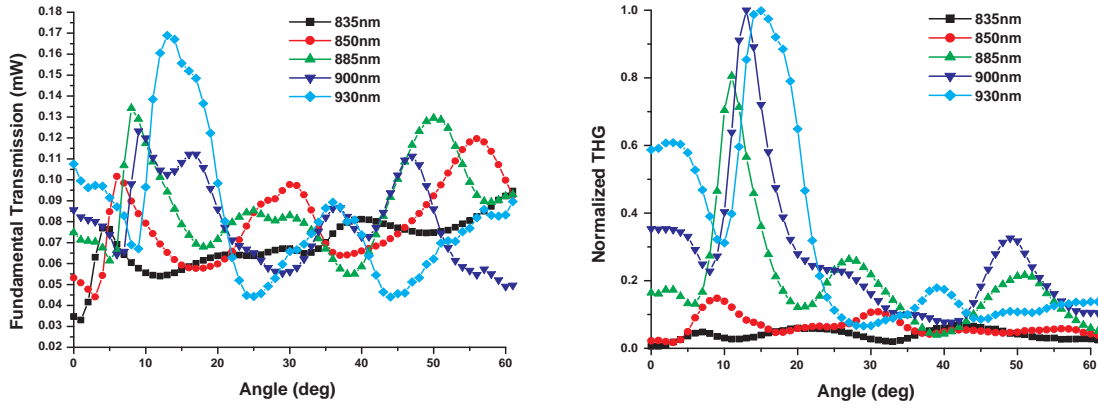


Figure 19: Fundamental transmission (left) and third-harmonic output (right) for samples of 250 nm apertures with variable spacing in a square lattice. The adhesion layer is 5 nm of TiO₂.

Two effects of changing the aperture spacing are readily observable. First, there is a shift to higher incidence angles at which the transmission/TH emission peak. Second, there is a clear increase in TH output for spacings of 885 nm and longer; note that this is repeatable across multiple measurements of these patterns. Even though the fundamental transmission peaks also increase with aperture spacing, the effect is not as dramatic.

4.2.2 Effects of aperture size

Keeping the aperture spacing fixed at about 885 nm, we investigated the effects of varying the aperture size. The results are shown in Figure 20. Again, there are two effects which are immediately noticed. The first is that the transmission of the fundamental increases with increasing aperture size, which is expected; however, the second effect is unexpected. At the first two peaks in TH output (near zero and 10°), TH *decreases* with aperture size, while at the third peak (near 30°), TH *increases* with aperture size; at the fourth peak, it decreases again. Individual apertures have cutoff frequencies, below which group velocity is minimized, resulting in increase in intra-aperture intensity [6, 37]. This suggests an explanation for the behavior seen at 0°, 10°, and 50°, where the decreasing aperture size should result in increasing TH. However, this doesn't explain the results at 30°. The fundamental difference between these two cases lies in the localization of the enhanced electromagnetic field.

In order to investigate the origin of the scaling of TH with aperture size, we performed calculations using Lumerical FDTD Solutions. Figure 21 shows the results of these calculations, where

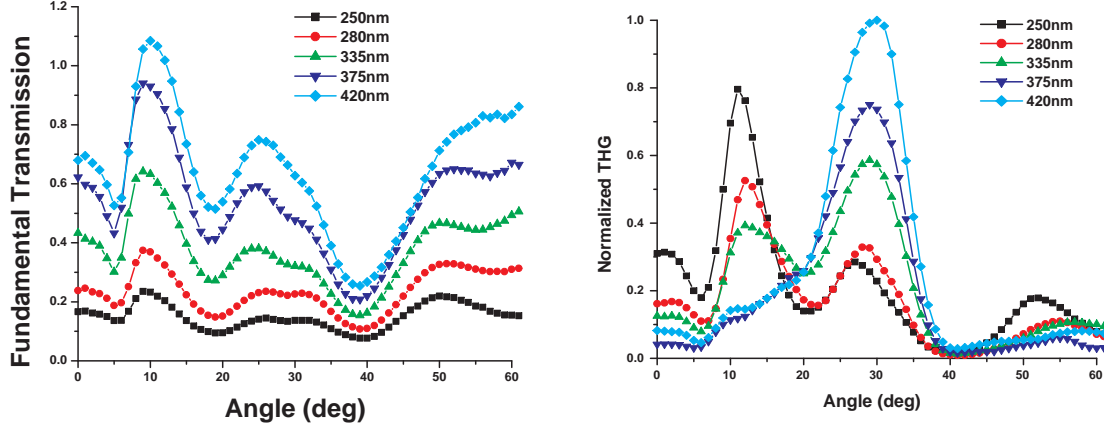


Figure 20: Fundamental transmission (left) and third-harmonic output (right) for samples of variable hole size with 885 nm spacing in a square lattice. The adhesion layer is 5 nm of TiO_2 .

transmission of the fundamental is plotted versus incidence angle for different aperture sizes. By comparing with Fig. 20, good agreement with experiment is obtained. The origin of the emitted TH signal is from the interior metal surface of the aperture and the substrate at the bottom of the aperture, where $E^3(\omega)$ at these locations is the source polarization. Figure 21 also plots the average value of E^3 within a volume that lies 10 nm from the interior surface of the aperture. As shown, the intensity increases with aperture size at 25° , but decreases at 10° , supporting the experimental measurements well.

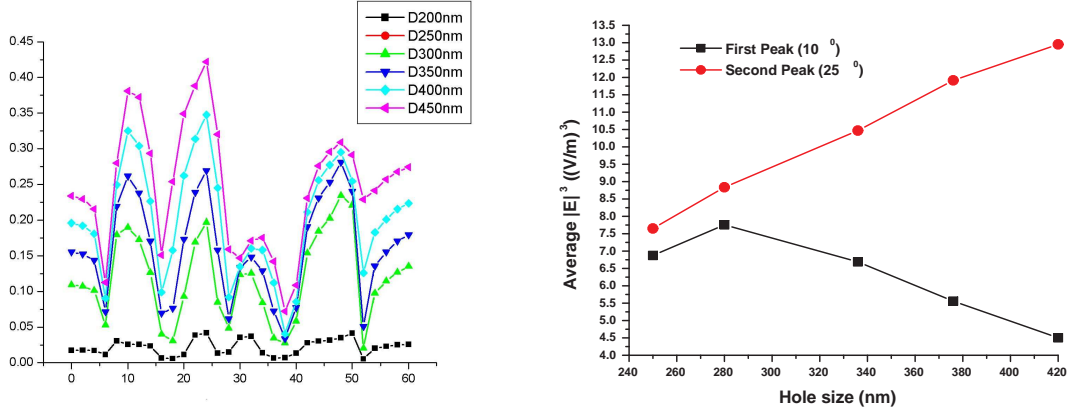


Figure 21: Calculated fundamental transmission versus incidence angle for different aperture diameters (left) with 885 nm spacing. Calculated average $|E|^3$ within a 10 nm thick bucket-shaped volume versus aperture size for angles of incidence corresponding to the second and third transmission resonance.

4.3 Conclusions

We have observed TH signal from arrays of sub-wavelength apertures. The peak TH is obtained at incidence angles corresponding to EOT of the fundamental, with signal strength comparable to SH under strong symmetry-breaking conditions. There is a clear effect of lattice spacing and aperture size on TH signal, where an anomaly is observed in the scaling of TH with aperture size at different

incidence angles corresponding to EOT.

Future work will focus on multi-photon luminescence, the prospects for super-continuum generation, and the incorporation of strongly nonlinear materials within the apertures, such as quantum dots.

References

- [1] V. Govindan and S. Blair “Limitations on nonlinear pulse propagation in coupled-resonator slow-light waveguides,” *Optics Express* **15**, 3922–3930 (2007).
- [2] V. Govindan and S. Blair “Nonlinear pulse interaction in microresonator slow-light waveguides,” *Journal of the Optical Society of America B* **25**, C23–C30 (2008).
- [3] V. Govindan and S. Blair “Analysis of optical array architectures in the slow-light regime,” *Journal of the Optical Society of America B* **25**, C116–C126 (2008).
- [4] J. Goeckeritz and S. Blair “One-dimensional photonic crystal rib waveguides,” *Lightwave Technology, Journal of* **25**, 2435–2439 (2007).
- [5] J. Goeckeritz and S. Blair “Optical characterization of coupled resonator slow-light rib waveguides,” *Optics Express* **18**, 18190–18199 (2010).
- [6] E. Popov, M. Nevière, J. Wenger, P.-F. Lenne, H. Rigneault, P. Chaumet, N. Bonod, J. Dintinger, and T. Ebbesen “Field enhancement in single subwavelength apertures,” *Journal of the Optical Society of America A* **23**, 2342–2348 (2006).
- [7] F. Mahdavi, Y. Liu, and S. Blair “Modeling fluorescence enhancement from metallic nanocavities,” *Plasmonics* **2**, 129–141 (2007).
- [8] T. Xu, X. Jiao, G. P. Zhang, and S. Blair “Second-harmonic emission from sub-wavelength apertures: Effects of aperture symmetry and lattice arrangement,” *Optics Express* **15**, 13894–13906 (2007).
- [9] T. Xu, X. Jiao, and S. Blair “Third-harmonic generation from arrays of sub-wavelength metal apertures,” *Opt. Express* **17**, 23582–23588 (2009).
- [10] L. V. Hau, S. E. Harris, Z. Dutton, and C. H. Behroozi “Light speed reduction to 17 metres per second in an ultracold atomic gas,” *Nature* **397**, 594–598 (1999).
- [11] A. Yariv, Y. Xu, R. K. Lee, and A. Scherer “Coupled-resonator optical waveguides: a proposal and analysis,” *Optics Letters* **24**, 711–713 (1999).
- [12] J. Heebner, R. W. Boyd, and Q.-H. Park “SCISSOR solitons and other novel propagation effects in microresonator-modified waveguides,” *Journal of the Optical Society of America B* **19**, 722–731 (2002).
- [13] A. Melloni, F. Morichetti, and M. Martinelli “Linear and nonlinear pulse propagation in coupled resonator slow-wave optical structures,” *Optical and Quantum Electronics* **35**, 365–379 (2003).
- [14] Y. Chen and S. Blair “Nonlinearity enhancement in finite coupled-resonator slow-light waveguides,” *Optics Express* **12**, 3353–3366 (2004).
- [15] M. A. Allen and G. S. Kino “On the theory of strongly coupled cavity chains,” *IEEE Transactions on Microwave Theory and Techniques* **8**, 362–372 (1960).
- [16] H. J. Curnow “A general equivalent circuit for coupled-cavity slow-wave structures,” *IEEE Transactions on Microwave Theory and Techniques* **13**, 671–675 (1965).

- [17] L. Maleki, A. B. Matsko, A. A. Savchenkov, and V. S. Ilchenko “Tunable delay line with interacting whispering-gallery-mode resonators,” *Optics Letters* **29**, 626–628 (2004).
- [18] R. W. Boyd, D. J. Gauthier, A. L. Gaeta, and A. E. Willner “Maximum time delay achievable on propagation through a slow-light medium,” *Physical Review A* **71**, (2005).
- [19] R. S. Tucker, P.-C. Ku, and C. J. Chang-Hasnain “Slow-light optical buffers: Capabilities and fundamental limitations,” *Journal of Lightwave Technology* **23**, 4046– (2005).
- [20] J. B. Khurgin “Optical buffers based on slow light in electromagnetically induced transparent media and coupled resonator structures: comparative analysis,” *Journal of the Optical Society of America B* **22**, 1062–1074 (2005).
- [21] F. G. Sedgwick, C. J. Chang-Hasnain, P. C. Ku, and R. S. Tucker “Storage-bit-rate product in slow-light optical buffers,” *Electronics Letters* **41**, 1347–1348 (2005).
- [22] Y. Chen, G. Pasrija, B. Farhang-Boroujeny, and S. Blair “Engineering the nonlinear phase shift using multi-stage auto-regressive moving-average optical filters,” *Applied Optics* **13**, 2564–2574 (2005).
- [23] G. Pasrija, Y. Chen, B. Farhang-Boroujeny, and S. Blair “DSP approach to the design of nonlinear optical devices,” *EURASIP Journal on Applied Signal Processing* **2005**, 1485–1497 (2005).
- [24] C. K. Madsen and J. H. Zhao *Optical Filter Design and Analysis: A Signal Processing Approach*. Wiley 1999.
- [25] S. Darmawan, Y. Landobasa, and M. Chin “Phase engineering for ring enhanced mach-zehnder interferometers,” *Optics Express* **13**, 4580–4588 (2005).
- [26] E. M. Dowling and D. L. MacFarlane “Lightwave lattice filters for optically multiplexed communication systems,” *Lightwave Technology, Journal of* **12**, 471–486 (1994).
- [27] K. Jinguji “Synthesis of coherent two-port optical delay line circuits with ring waveguides,” *Journal of Lightwave Technology* **14**, 1882–1898 (1996).
- [28] A. Melloni and M. Martinelli “Synthesis of direct-coupled-resonators bandpass filters for WDM systems,” *Journal of Lightwave Technology* **20**, 296–303 (2002).
- [29] T. W. Ebbesen, H. J. Lezec, H. F. Ghaemi, T. Thio, and P. A. Wolff “Extraordinary optical transmission through sub-wavelength hole arrays,” *Nature* **391**, 667–669 (1998).
- [30] L. Salomon, F. Grillot, A. V. Zayats, and F. Fornel “Near-field distribution of optical transmission of periodic subwavelength holes in a metal film,” *Physical Review Letters* **86**, 1110–1113 (2001).
- [31] Y. Liu and S. Blair “Fluorescence enhancement from an array of sub-wavelength metal apertures,” *Optics Letters* **28**, 507–509 (2003).
- [32] A. Nahata, R. A. Linke, T. Ishi, and K. Ohashi “Enhanced nonlinear optical conversion using periodically nanostructured metal films,” *Optics Letters* **28**, 423–425 (2003).

- [33] N. Rakov, F. E. Ramos, and M. Xiao “Strong second-harmonic generation from a thin silver film with randomly distributed small holes,” *Journal of Physics: Condensed Matter* **15**, L349–L352 (2003).
- [34] M. Airola, Y. Liu, and S. Blair “Second-harmonic generation from an array of sub-wavelength metal apertures,” *Journal of Optics A* **7**, S118–S123 (2005).
- [35] W. Fan, S. Zhang, N. C. Panoiu, A. Abdenour, S. Krishna, J. R. M. Osgood, K. J. Malloy, and S. R. J. Brueck “Second-harmonic generation from a nanopatterned isotropic nonlinear material,” *Nano Letters* **6**, 1027–1030 (2006).
- [36] A. Lesuffleur, L. K. S. Kumar, and R. Gordon “Enhanced second harmonic generation from nanoscale double-hole arrays in a gold film,” *Applied Physics Letters* **88**, 261104 (2006).
- [37] J. A. H. van Nieuwstadt, M. Sandtke, R. H. Harmsen, F. B. Segerink, J. C. Prangsma, S. Enoch, and L. Kuipers “Strong modification of the nonlinear optical response of metallic subwavelength hole arrays,” *Physical Review Letters* **97**, 146102 (2006).
- [38] A. Lesuffleur, L. K. S. Kumar, and R. Gordon “Apex-enhanced second harmonic generation by using double-hole arrays in a gold film,” *Physical Review B* **75**, 045423 (2007).
- [39] P. Mülschlegel, H.-J. Eisler, O. J. F. Martin, B. Hecht, and D. W. Pohl “Resonant optical antennas,” *Science* **308**, 1607–1609 (2005).
- [40] S. Kim, J. Jin, Y.-J. Kim, I.-Y. Park, Y. Kim, and S.-W. Kim “High-harmonic generation by resonant plasmon field enhancement,” *Nature* **453**, 757–760 (2008).
- [41] X. Jiao, J. Goeckeritz, S. Blair, and M. Oldham “Localization of near-field resonances in bow-tie antennae: influence of adhesion layers,” *Plasmonics* **4**, 37–50 (2009).
- [42] H. Aouani, J. Wenger, D. Gerard, H. Rigneault, E. Devaux, T. W. Ebbesen, F. Mahdavi, T. Xu, and S. Blair “Crucial role of the adhesion layer on the plasmonic fluorescence enhancement,” *ACS Nano* **3**, 2043–2048 (2009).